JOURNAL OF SPACECRAFT AND ROCKETS
Vol. 36, No. 6, November–December 1999

Euler and Navier–Stokes Solutions for Missiles at High Angles of Attack

E. Oktay,* N. Alemdaroğlu,† and E. Tarhan‡
ROKETSAN, Missiles Industries, Inc., 06780 Ankara, Turkey
and
P. Champigny§ and P. d'Espiney¶
ONERA, F-92322 Chatillon CEDEX, France

An unstructured Euler flow solver and a structured thin-layer Navier–Stokes solver are validated against experimental data and compared with other solvers for two different missile geometries at a Mach number of $M = 2$ and at angles of attack ranging between 0 and 20 deg. The first geometry is a conventional missile geometry with an ogive nose, a cylindrical body, and four straight tail fins. The second geometry is an unconventional missile geometry with a lenticular body and no tail fins. Present results are found to be in good agreement with the available results, and the differences observed between them are explained in detail. The present unstructured Euler code proved to be accurate, fast, and reliable for determining the overall aerodynamic characteristics of the missiles, whereas the thin-layer Navier–Stokes solutions are found to be effective in predicting the detailed viscous behavior of the flowfield over the conventional and unconventional missile geometries studied.

Nomenclature

C_m = pitch moment coefficient
C_N = normal force coefficient
C_p = pressure coefficient
c = chord length of the fin
D = missile diameter
e = total energy per unit volume
$\boldsymbol{f}, \boldsymbol{g}, \boldsymbol{h}$ = inviscid flux vectors in transformed coordinates
h = exposed half span of the fin
L = axial missile length
M_∞ = freestream Mach number
$\boldsymbol{n}$ = surface normal unit vector
p = pressure
$\boldsymbol{Q}$ = vector of conservative variables
Re_D = Reynolds number based on the diameter D, $V_\infty D/\nu_\infty$
Re_L = Reynolds number based on the length L, $V_\infty L/\nu_\infty$
S = cross-sectional area
$\boldsymbol{s}$ = viscous flux vector
t = thickness of the fin
t = time
u, v, w = velocity components in x, y, and z directions
X_{cp} = x location of the center of pressure
x, y, z = axial, lateral, and vertical coordinates
Y_{cp} = y location of the center of pressure
α = angle of attack
γ = ratio of specific heats
ξ, η, ζ = transformed coordinates
ρ = density
υ = dimensionless time

Subscript

x, y, z = Cartesian components

Received 2 June 1998; revision received 10 June 1999; accepted for publication 15 June 1999. Copyright © 1999 by the American Institute of Aeronautics and Astronautics, Inc. All rights reserved.

*Chief Engineer, Engineering Development Department, Elmadağ.
†Consultant, Engineering Development Department, Elmadağ; also Professor of Aeronautical Engineering Department, Middle East Technical University, 06531 Ankara, Turkey.
‡Engineer, Engineering Development Department, Elmadağ.
§Head of Missiles, Hypersonic and Space Unit, Applied Aerodynamics Department.
¶Senior Research Engineer, Missiles and Aircraft Division, Applied Aerodynamics Department.

Introduction

COMPUTATIONAL fluid dynamics (CFD) has become a very important and effective design tool in aerodynamics research. Besides reducing the time required for expensive wind-tunnel testing, CFD can provide additional insight to the analysis and design of aerodynamic vehicles. Today CFD has become a standard and an inevitable design tool for the aerodynamicist. Although the computational time increases with the geometrical complexity of the vehicle, it is still much less expensive to obtain solutions by CFD methods as compared to experimental work. One of the important applications of CFD is definitely the design of missiles.

An unstructured three-dimensional Euler solver,[1,2] USER3D, is developed and used extensively as a design tool for predicting as well as for improving the performances of missiles. The reliability of any kind of flight simulation for missiles depends on the accuracies with which the aerodynamic coefficients of the complex missile geometries are predicted. Hence, the results of CFD predictions must be carefully tuned and validated against available experimental data such that they can be applied without any ambiguity and questions. The starting point of this research was to validate the USER3D and thin-layer Navier–Stokes (TLNS) codes against experimental data and other available CFD codes. In particular, these codes will be validated for applications at high Mach numbers and at high angles of attack.

Schiff and Steger[3] solved supersonic high-incidence turbulent flow using a parabolized Navier–Stokes method and a modified Baldwin–Lomax turbulence model.[4] Schiff et al. also applied a time-marching TLNS code to compute laminar and turbulent flow over bodies at large angles of attack.[5] Physical aspects governing accurate numerical simulation of turbulent flows over bodies at large incidence are also reexamined in Ref. 6.

In the current work, two different missile geometries are studied at high angles of attack. The first one is a conventional missile geometry with an ogive nose, a cylindrical body, and four straight tail fins on which experimental studies were performed previously at ONERA (Champigny, private communication, March 1996). The second one is an unconventional missile geometry with a lenticular body shape and no tail fins. This geometry was previously investigated by d'Espiney,[7] using different computational methods such as a panel method and a semi-empirical method, as well as ONERA's Euler code. Reference 7 also details the experimental investigations performed on this geometry and compares the computational results with experimental data. Further computations on the same geometry using the thin-layer and space-marching Navier–Stokes solvers are performed, and the results were compared with the Euler and

experimental results.[8] Further studies on the same geometry using the three-dimensional laminar and two-dimensional turbulent computations with the Navier–Stokes solver called FLU3M are also given by Jouet and d'Espiney.[9] The details of the experiments carried out at ONERA on this model are also reported.[10]

The results of the Euler computations that will be given in this paper were previously presented in detail.[2] Although the main emphasis here will be mostly on the computations performed by the TLNS solver, the same Euler computations will also be presented for the sake of completeness of the discussions. All of the Euler computations are performed at a freestream Mach number of $M_\infty = 2.0$ and at different angles of attack α, $0 \text{ deg} \leq \alpha \leq 20$ deg. On the other hand, TLNS computations are presented only for some selected cases: for the conventional missile geometry $M = 2.0$, $\alpha = 5$ and 10 deg, and for the lenticular body, $M = 2.0$, $\alpha = 10$ deg. The computational results obtained by USER3D and TLNS for each of the test cases are compared with each other, as well as with the computational results of FLU3M.[7–9] All of these results are then compared with the experimental results of ONERA. In general, it is observed that the predictions of the unstructured Euler and the TLNS codes are in good agreement with both the numerical and the experimental results of ONERA.

USER3D Flow Solver

The unstructured Euler flow solver USER3D that is used in this study was developed at ROKETSAN, and details about the code are given in Refs. 1 and 2. This code employs a fully conservative, cell-centered, finite volume method applied to the tetrahedral cells of the computational grid. Second-order spatial discretization is based on Roe's flux difference splitting method.[11] An m-stage Runge–Kutta time-stepping scheme[12] is used for time integration. Local time stepping and implicit residual smoothing accelerate convergence to steady state.

Higher-order interpolation and reconstruction schemes together with a total variation diminishing limiter scheme are incorporated into the code to enhance the numerical accuracy of the computations. In this way, higher-order accuracy in space is obtained even in highly stretched grids.

Governing Equations

The time-dependent Euler equations for an ideal compressible fluid in the absence of external forces are given in integral form as

$$\frac{\partial}{\partial t}\iiint_{\Omega} \boldsymbol{Q}\,\mathrm{d}V + \iint_{\partial\Omega} \boldsymbol{F}(\boldsymbol{Q})\cdot\boldsymbol{n}\,\mathrm{d}S = 0 \tag{1}$$

where Ω represents the physical domain with a boundary $\partial\Omega$. The vectors $\boldsymbol{Q}$ and $\boldsymbol{F}$ are given by

$$\boldsymbol{Q} = \begin{Bmatrix} \rho \\ \rho u \\ \rho v \\ \rho w \\ e \end{Bmatrix}, \qquad \boldsymbol{F}(\boldsymbol{Q})\cdot\boldsymbol{n} = (\boldsymbol{V}\cdot\boldsymbol{n}) \begin{Bmatrix} \rho \\ \rho u \\ \rho v \\ \rho w \\ e+p \end{Bmatrix} + p \begin{Bmatrix} 0 \\ n_x \\ n_y \\ n_z \\ 0 \end{Bmatrix} \tag{2}$$

where n_x, n_y, and n_z are the Cartesian components of the exterior surface unit normal $\boldsymbol{n}$ on the boundary $\partial\Omega$. Pressure can be expressed as

$$p = (\gamma - 1)\left[e - \tfrac{1}{2}\rho(u^2 + v^2 + w^2)\right] \tag{3}$$

Boundary Conditions

A flow tangency condition was imposed on the walls and symmetry planes by setting the velocities on the boundary faces to their cell-center values and then subtracting the component normal to the solid surface. Density and pressure boundary conditions were simply set to the cell-centered values.

Characteristic boundary conditions were applied to the far-field boundary for each computation using the fixed and extrapolated Riemann invariants corresponding to the incoming and outgoing waves. The incoming Riemann invariant is determined from the freestream flow, and the outgoing invariant is extrapolated from the interior domain. The invariants are used to determine the locally normal velocity component and the speed of sound. At the outflow boundary, the two tangential velocity components and the entropy were extrapolated from the interior, whereas at the inflow boundary, they were specified as having the far-field values. These five quantities provide a complete definition of the flow in the far field.

TLNS Flow Solver

The three-dimensional structured TLNS solver that was used in this study is a multiblock finite difference flow solver with second-order accuracy in space and time. This code uses the implicit approximate factorization algorithm of Beam and Warming[13] and a diagonalization procedure with similarity transformation suggested by Pulliam and Chaussee.[14] An alternating direction implicit method with lower and upper bidiagonalization is applied in the matrix solution. This flow solver is also capable of using variable time stepping for faster convergence to steady-state solutions. The dissipation model includes fourth-order explicit and second-order implicit smoothing terms (see Ref. 15 for further details). The original Baldwin–Lomax turbulence model is incorporated into the code for turbulent flow calculations.

Governing Equations

For the TLNS equations, the viscous effects in the directions along the solid boundary are neglected compared with those in normal direction to the solid boundary. Because of this assumption, the TLNS equations can be expressed in the generalized curvilinear coordinates (ξ, η, ζ) as

$$\frac{\partial \boldsymbol{Q}}{\partial \upsilon} + \frac{\partial \boldsymbol{f}}{\partial \xi} + \frac{\partial \boldsymbol{g}}{\partial \eta} + \frac{\partial \boldsymbol{h}}{\partial \zeta} = \frac{1}{Re_\infty}\frac{\partial s}{\partial \zeta} \tag{4}$$

The details of the formulation can be found in Ref. 15.

Boundary Conditions

Adiabatic walls and no-slip boundary conditions are imposed for solid boundaries. Pressure is obtained from the normal momentum equation, and the energy is updated by using the wall pressure. For supersonic inflow, the flow variables are taken from the freestream values, and for supersonic outflow, the flow variables are extrapolated from the computational domain. A three-point linear interpolation technique is used for matching the surface conditions in the multiblock cases.

Grid Generation

The unstructured grids used for the Euler computations were generated using I-DEAS™. Although this tool is not very convenient for generating grids suitable for our present studies, various control features of the code are used until an appropriate grid distribution is achieved. One of the basic advantages of using this tool for grid generation lies in that the geometry directly comes from this design package. Thus, any major modification made to the external geometry of the missile is passed directly to the CFD analysis. To get nearly the same grid distribution as in the ONERA studies, another in-house grid generation code was used. Although this is a structured grid generation code, it has the capability of generating structured tetrahedral grids with appropriate grid interconnectivity suitable for interfacing with the USER3D code.[2]

The grids used for TLNS computations are provided by ONERA, and therefore they are the same grids as used in their computations.[8,9] To observe the effect of grid size on viscous calculations two different grids were generated for the lenticular body. They were $59 \times 91 \times 70$ and $59 \times 91 \times 85$ points in axial, circumferential, and radial directions, respectively. The sensitivity of computations on the grid sizes will be discussed in the next section.

Results and Discussion

Conventional Missile

The geometry for the conventional missile is shown in Fig. 1. The missile has a three-caliber tangent ogive nose section followed by a cylindrical body and four straight cruciform tail fins. The fins have

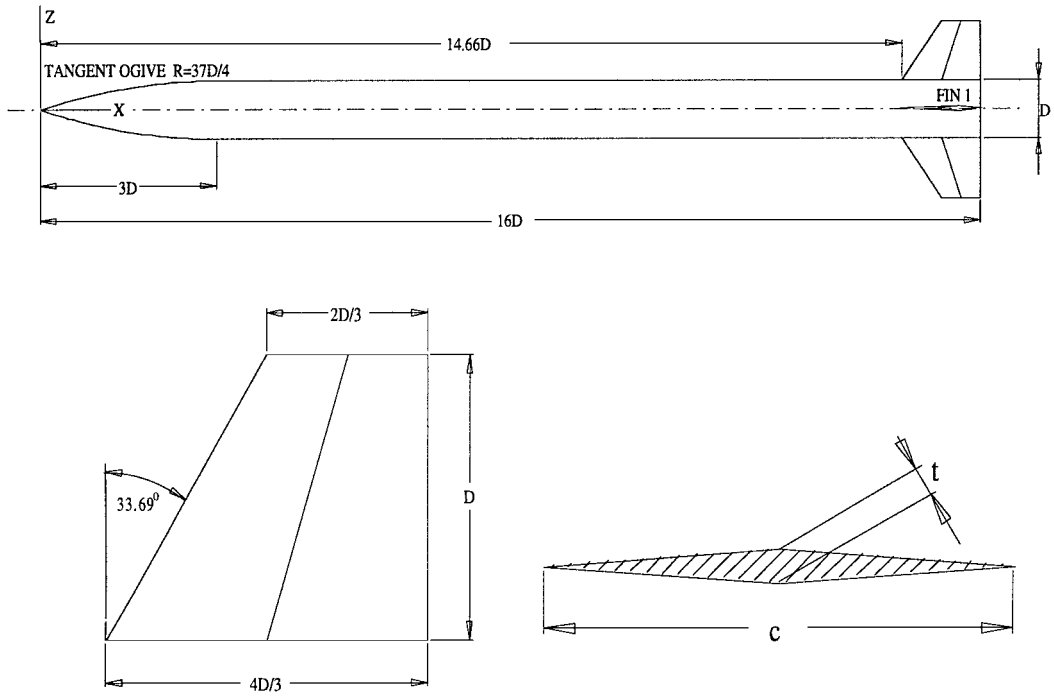

Fig. 1 Conventional missile geometry with four tail fins.

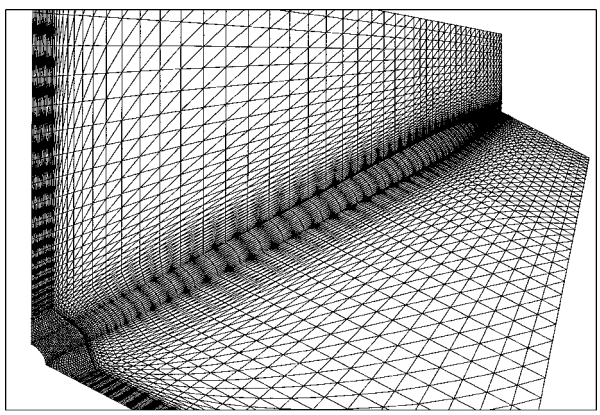

a) Unstructured Euler grid

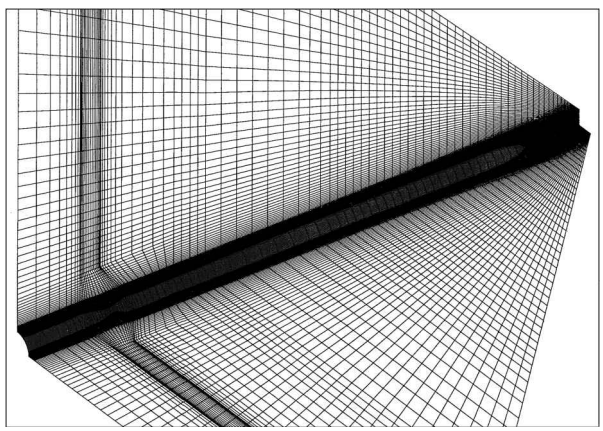

b) Structured Navier–Stokes grid

Fig. 2 Grids for the conventional missile geometry.

a constant thickness ratio of $t/c = 0.07$ along their span. The unstructured Euler grid generated for this geometry has 297,164 cells with 54,029 nodes and 603,129 faces for half-body and is shown in Fig. 2a. The structured grid used for the TLNS solutions is shown in Fig. 2b, which is the same grid used by ONERA. The ogive-cylinder body is defined by two blocks, each composed of $54 \times 73 \times 85$ grid points. The tail fin region is divided into four blocks, each having $40 \times 37 \times 85$ grid points. All of the Euler computations are performed at a freestream Mach number of $M_\infty = 2.0$ and at different angles of attack α, 0 deg $\leq \alpha \leq$ 20 deg. On the other hand, TLNS computations are presented only for some selected cases: $M = 2.0$, $\alpha = 5$ and 10 deg, $Re = 0.7 \times 10^6$ (based on missile diameter) and for turbulent flow. The complete flowfield around the missile calculated by the Euler solver USER3D is presented in Fig. 3 for $M = 2.0$ and $\alpha = 20$ deg as iso-Mach contours. Figure 4 shows the variation of the normal force coefficient C_N with angle of attack α. The results of Euler computations are compared with those of experiments as well as with the results of FLU3M. The TLNS results for 10 and 20 deg are also plotted in Fig. 4. It is observed that all of the results are in very good agreement until 5-deg angle of attack, after which the present results overestimate and the FLU3M results underestimate the experimental values. However, the present Euler and TLNS results are observed to be much closer to the experimental data. The increasing discrepancy between the computational and the experimental results can be attributed to viscous effects becoming dominant, especially at high angles of attack. The comparison of the FLU3M result with experimental data at 20-deg angle of attack is fortuitous for an inviscid Euler solution. The variation of the pitching moment coefficient about the $8D$ axial position with respect to the angle of attack is given in Fig. 5. Remarkably good agreement between all of the methods used and the experimental values are

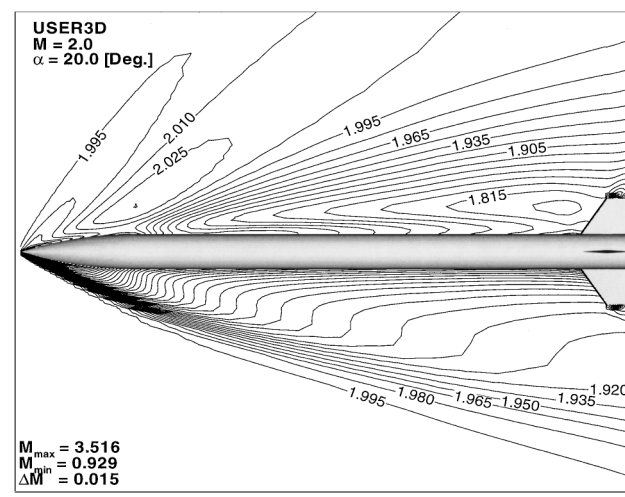

Fig. 3 Mach contours (USER3D) at M = 2.0 and α = 20 deg.

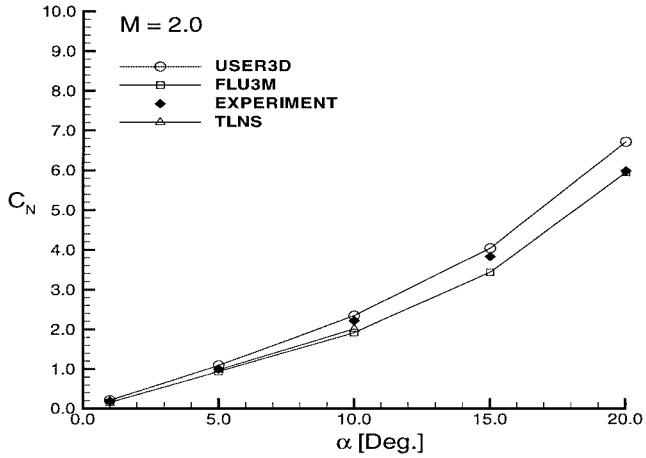

Fig. 4 Variation of normal force coefficient with angle of attack.

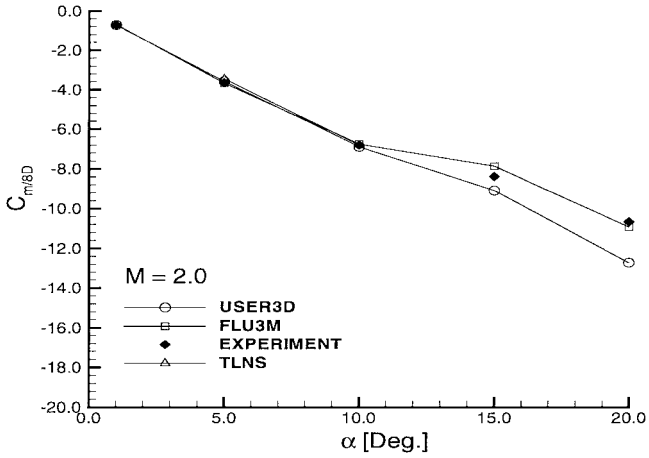

Fig. 5 Variation of pitching moment coefficient about $X/D = 8$ location.

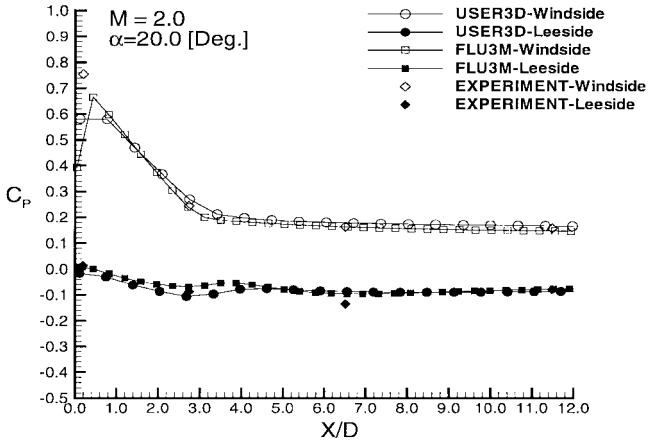

Fig. 6 Variation of pressure coefficient on the surface with axial distance.

observed up to 10-deg angle of attack, after which both of the solutions are observed to deviate from the experimental data due to the inherent behavior of Euler solutions at high angles of attack. The distribution of pressure coefficient C_p with axial distance x/D, at 20-deg angle of attack, both on the windward and on the leeward sides of the missile surface are given in Fig. 6 up to a distance of $12D$, which is just prior to the fin location. The two Euler results (USER3D and FLU3M) are in good agreement between each other, as well as with the experimental data. At this high angle of attack, the body vortices interact with the tail fins, and the flow around the

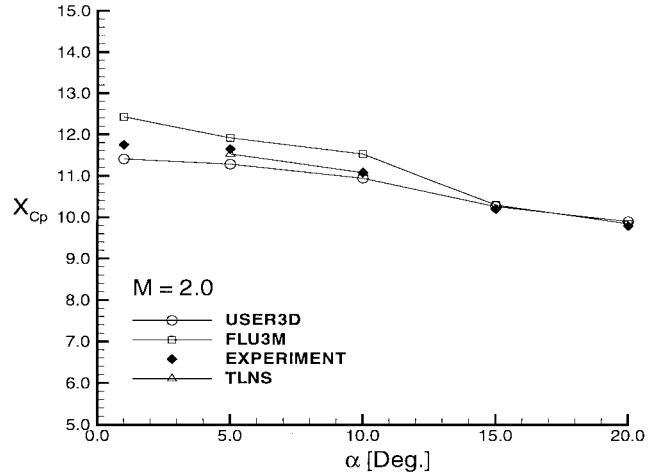

Fig. 7 Variation of the axial location of center of pressure with angle of attack.

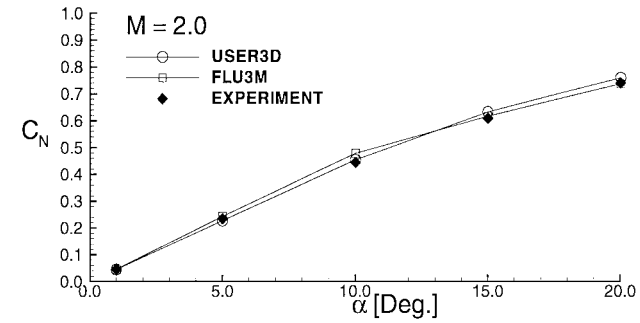

Fig. 8 Variation of normal force coefficient for fin 1 with angle of attack.

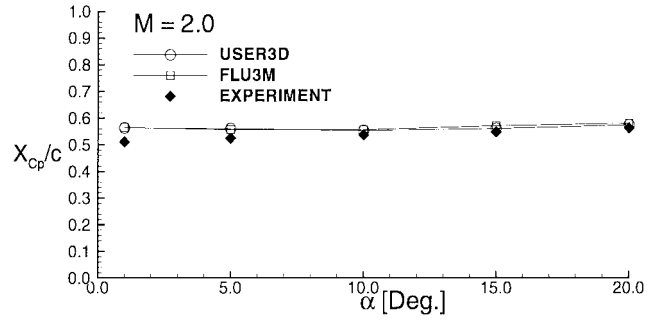

Fig. 9 Variation of axial location center of pressure for fin 1 with angle of attack.

tail fins will be governed by these vortices. These complicated flow phenomena explain the differences observed between the Euler computations and the experiments at high angles of attack ($\alpha = 20$ deg) in Figs. 4–6. Variation of the center of pressure location in the axial direction at different angles of attack is given in Fig. 7. Here USER3D underpredicts and FLU3M overpredicts the X_{cp} locations up to 15-deg angle of attack, after which all of the values coincide. This behavior can be explained by the cancellations of the opposing predictions observed in C_m and C_N coefficients due to the definition of X_{cp} being proportional to the ratio of C_m to C_N.

Results for the individual fin aerodynamic characteristics are now shown. Figure 8 shows the predictions of C_N for fin 1. The agreement between the two computational methods and the experimental data are very good for all of the angles of attack studied. The variation of the center of pressure location, X_{cp}, for this fin is given in Fig. 9. Both of the computational methods slightly overpredict the experimental data. The maximum difference is around 6% of the base chord and decreases with increasing angle of attack. This behavior is exactly opposite to the behavior observed in Fig. 10, which shows

the variation of Y_{cp} with respect to angle of attack. Both of the numerical methods underpredict the experimental data for this case. The maximum difference is around 3% of the base chord of the fin. It should be noted that Y_{cp} is measured from the centerline of the missile, whereas X_{cp} is measured from the tip of the root chord. For overall C_N and center of pressure location calculations, the cross-sectional area of the body is used as the reference area, whereas for the fins, the fin planform area is used as the reference area.

Unconventional Missile

The geometry of the unconventional missile is shown in Fig. 11. The unstructured grid used for Euler computations is given in Fig. 12a. This grid was generated by using I-DEAS and has 297,778 cells, 55,667 nodes, and 605,379 faces for a half-body. The structured Navier–Stokes grid generated for this unconventional lenticular body geometry is given in Fig. 12b. This grid was provided by ONERA and is the same grid that was used in their Navier–Stokes calculations,[8] consisting of $59 \times 91 \times 85$ grid points.

All of the Euler computations are performed at a freestream Mach number of $M_\infty = 2.0$ and at different angles of attack α, $0 \text{ deg} \le \alpha \le 20$ deg. On the other hand, TLNS computations are presented for $M = 2.0$, $\alpha = 10$ deg, and $Re = 3 \times 10^6$ (based on missile length). The normal force coefficient variation with angle of attack as calculated by the Euler and TLNS solvers is presented in Fig. 13. The results of Euler computations of ONERA, as well as their experimental results, are also plotted in Fig. 13. Navier–Stokes computations are performed for only one angle of attack, $\alpha = 10$ deg. Contrary to our expectations, and regardless of its deficiency in depicting the complete physical features of the flowfield, the results of the Euler codes are observed to be in good agreement with the experimental data. The same behavior is observed in Fig. 14, where the surface pressure coefficients calculated by the Euler methods are plotted for $\alpha = 20$ deg. In Fig. 14, one can also see the close match between the Euler computations and the experiments on the windward and the leeward sides except for the separated regions near and behind the sharp edges of the lenticular body. All of the aerodynamic coefficients are defined using the base cross-sectional area ($S_{base}/L^2 = 0.004176$) as the reference area.

The overall flowfield around the lenticular body as calculated by the TLNS solver is shown in Fig. 15 with iso-Mach contour plots

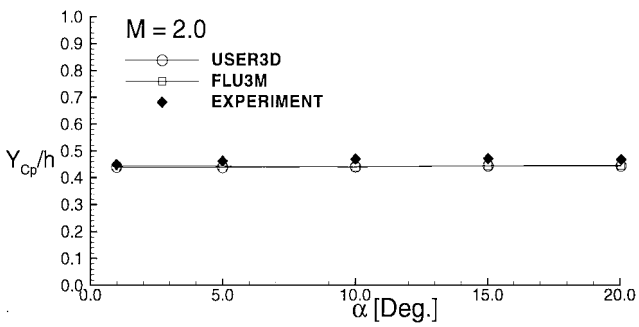

Fig. 10 Variation of y location center of pressure for fin 1 with angle of attack.

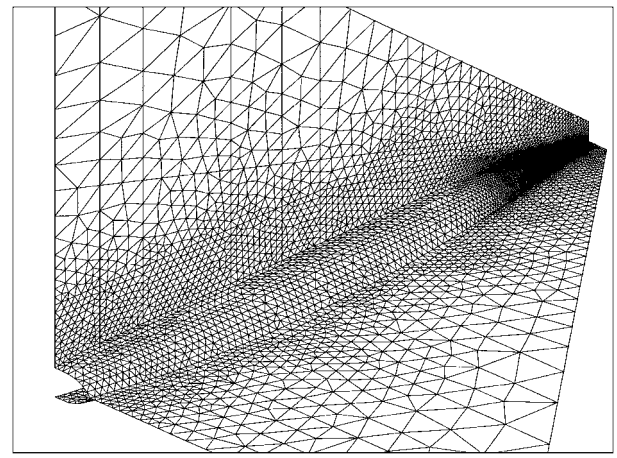

a) Unstructured Euler grid

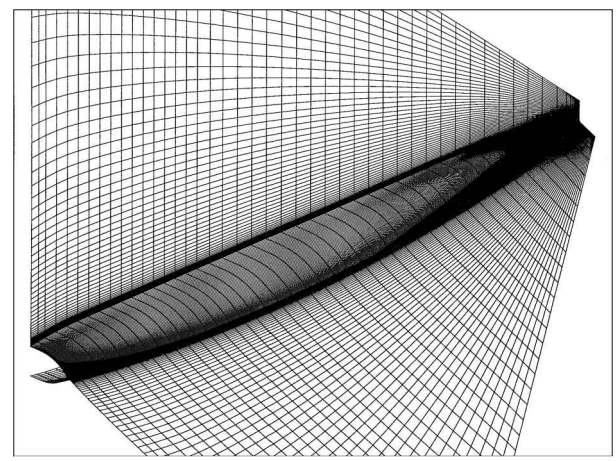

b) Structured Navier–Stokes grid

Fig. 12 Grids for the unconventional missile geometry.

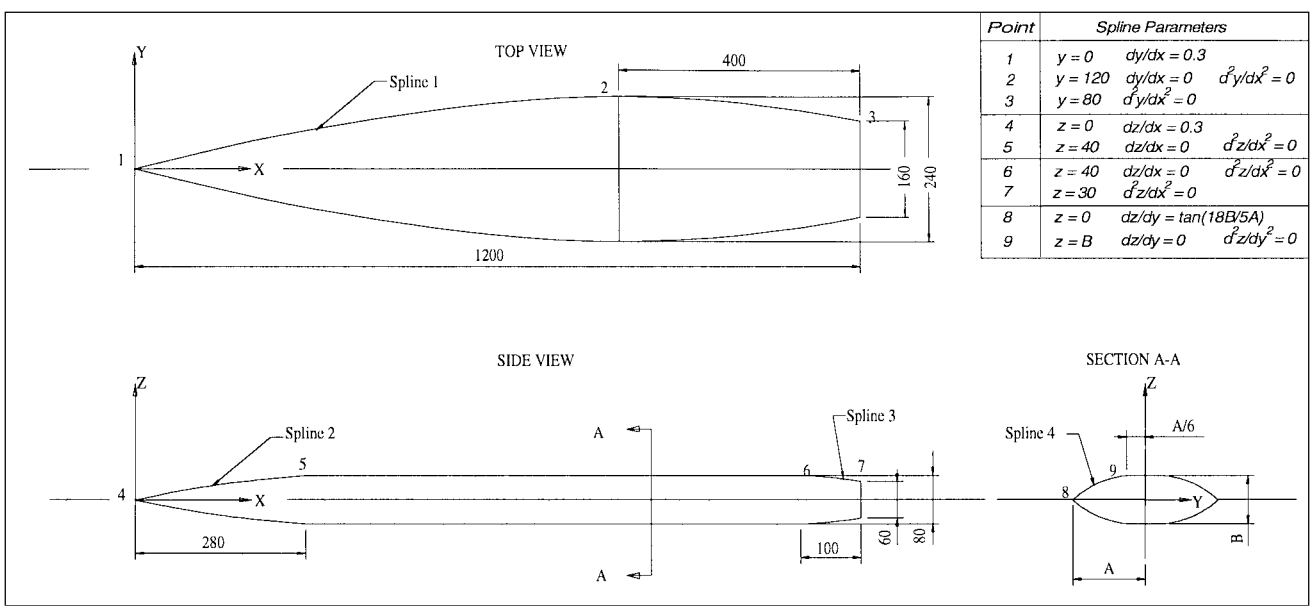

Fig. 11 Unconventional missile geometry having lenticular cross section.

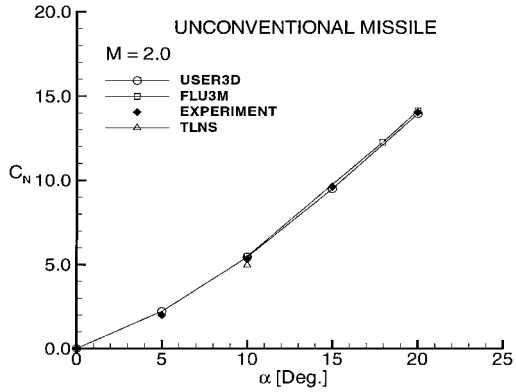

Fig. 13 Variation of normal force coefficient with angle of attack for the lenticular body.

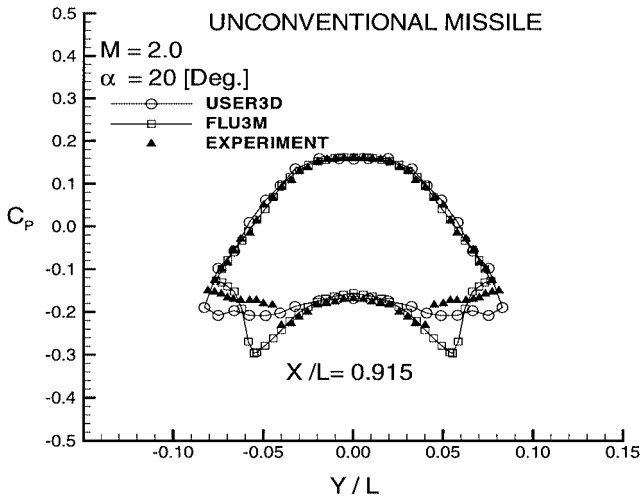

Fig. 14 Pressure coefficient distribution on the surface at a crossflow plane located at *X/L* = 0.915.

at an angle of attack of $\alpha = 10$ deg. This prediction is in very good agreement with those of Euler computations[2] and those of experimental data.[10] At this angle of attack, more interesting is the vortical flow structure on the leeward side of the body. The detail of this vortical flow is shown in Fig. 16 as iso-stagnation pressure contour plots at various crossflow planes. The complete and detailed evolution of the vortical flow pattern on the leeward surface is clearly shown in Fig. 17. Initially there is a single vortex closer to the vertical central plane (xz plane) of the body (inner vortex) that subsequently evolves into a double corotating vortex with the addition of a secondary outer vortex (the sharp edge vortex) at around $x/L = 0.571$. Farther downstream, this vortex outgrows the first vortex at a faster rate and eventually merges with it at about $x/L = 0.62$. The merger of these two vortices accelerates the growth rate of this single unified vortex, giving rise to a secondary small counter-rotating vortex at about the same location as the merger. Farther downstream one can observe the pairing of these secondary counter-rotating vortices at around $x/L = 0.756$.

Figures 18a and 18b show the experimental surface oil flow visualization and computed surface skin friction lines along the leeward side of the lenticular body. One can observe the close agreement of separation and reattachment lines from the experiments and computations. A possible interpretation for the reattachment and separation lines observed at $x/L = 0.571$ can be given in conjunction with the crossflow vortical structure in this plane. The schematic representation of the flow is given in Fig. 18c. The two corotating vortices, designated as F_1 and F_3, are the inner and outer vortices. The flow separates from the sharp edge of the body (separation line S_1), reattaches at the centerline as R_1, and follows the surface. Reattachment line R_2 and separation line S_2 are both related to the secondary counter-rotating vortex F_2. Although the innermost line (line C)

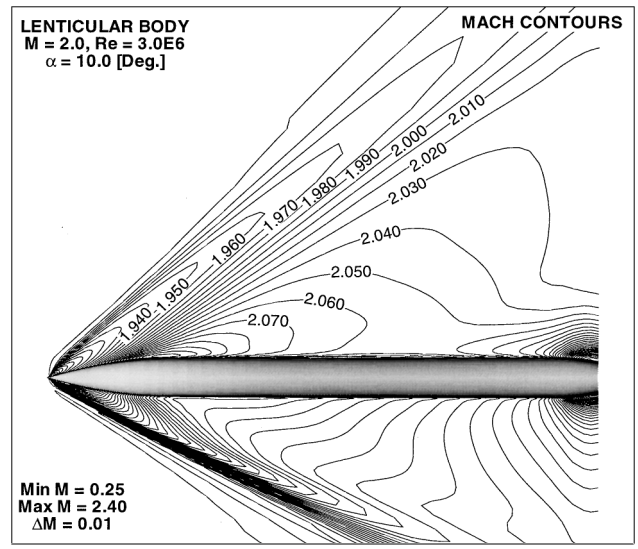

a) Side view

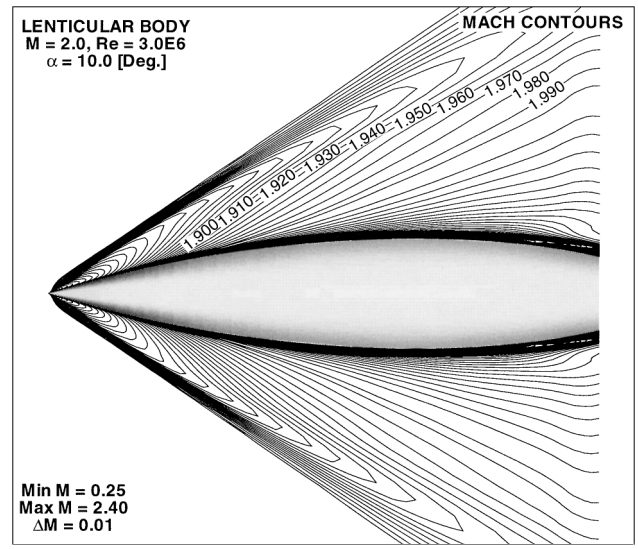

b) Top view

Fig. 15 Iso-Mach lines (TLNS) around the unconventional missile.

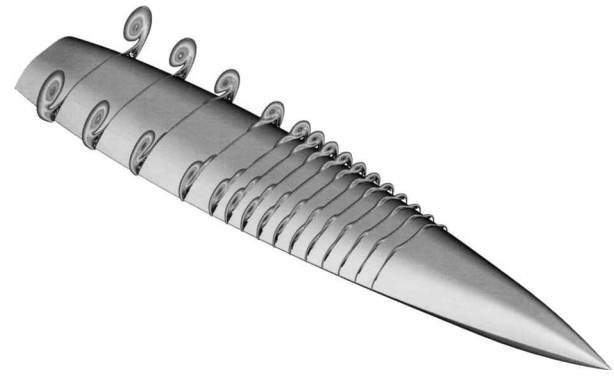

Fig. 16 Iso-stagnation pressure contours (TLNS) on the unconventional missile: *M* = 2.0, α = 10.0 deg, and $Re_L = 3.0E6$.

can be thought as another separation line, it is interpreted as concentrated surface skin friction lines.[8] The extent of line C given by the computations in Fig. 18b is shorter than what is observed experimentally in the oil flow visualization in Fig. 18a. Full Navier–Stokes solutions of ONERA[9] gave a larger extent for this line C that agreed better with the oil flow visualizations. Therefore, it is likely that the present results would be better if the computations were performed with an appropriate turbulence model. Schiff et al.[5] have reported on

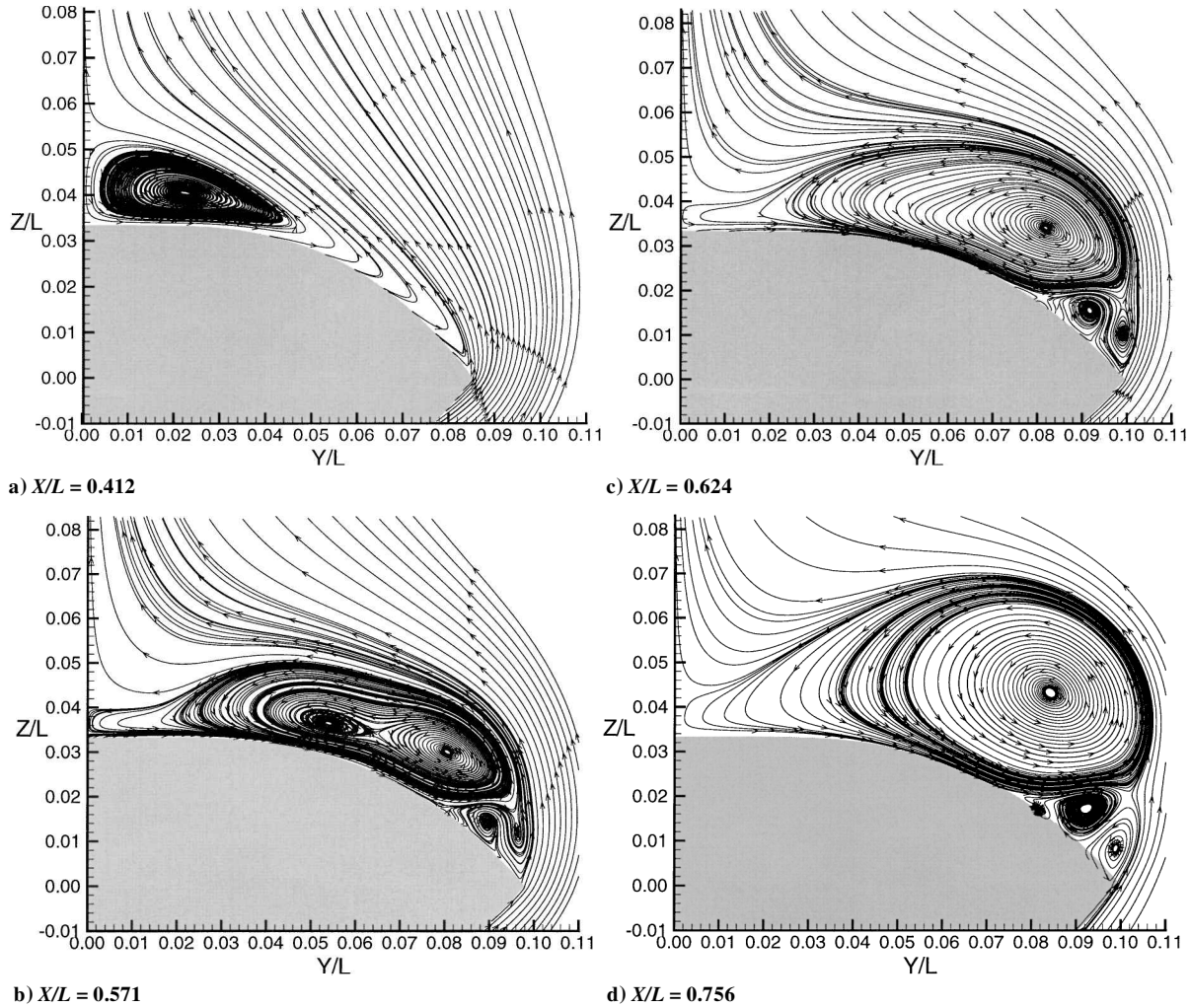

Fig. 17 TLNS solutions showing crossflow streamlines at various planes.

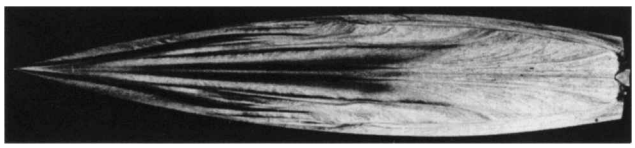

a) Experiment

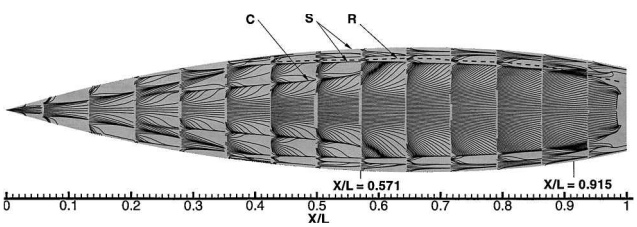

b) TLNS solution

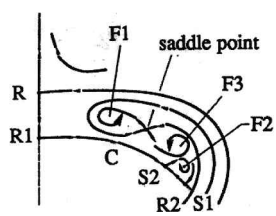

c) Crossflow organization

Fig. 18 Surface skin friction lines: R, reattachment; S, separation; C, concentrated streamlines; and F, vortices.

the effects of grid resolution and turbulence model on the primary and secondary crossflow separation lines. They have corrected the physically unrealistic case of a primary crossflow separation line originating from the nose and becoming the secondary crossflow separation line on the aft portion of the body by doubling the circumferential grid resolution. With this modification, they were able to obtain a primary crossflow separation line that ran the total length of the body. Although in the present study two different grid distributions were used, grid refinement was mainly performed in the radial direction, increasing from 70 to 85 points, to compensate for boundary-layer effects; no grid refinement was done in the circumferential direction. Such a refinement would be much more effective to resolve the vortical flow structure on the leeward side of the body. The comparison of calculated and experimental surface pressure coefficients is given in Figs. 19a and 19b for $x/L = 0.571$ and 0.915, respectively, for the 10-deg angle-of-attack case. Although the general behavior of the pressure coefficients is well predicted with the TLNS computations, discrepancies are observed, in particular on the leeward side of the missile. At $x/L = 0.571$, the two corotating vortices on the leeward side are clearly evidenced by the two suction peaks. Although the measured suction peak corresponding to the outer vortex (sharp edge vortex) is more pronounced than the computed values, this behavior is exactly reversed for the inner vortex, where the experimental values are lower than the computational predictions. At $x/L = 0.915$, the C_p distribution is completely different and the windward pressure coefficient falls below that of the leeward value around the sharp edge, most probably due to the boattail effect and the separation of flow from the sharp edge. The differences observed in the C_p values between the experiments and the calculations can be explained in terms of the deficiency of the

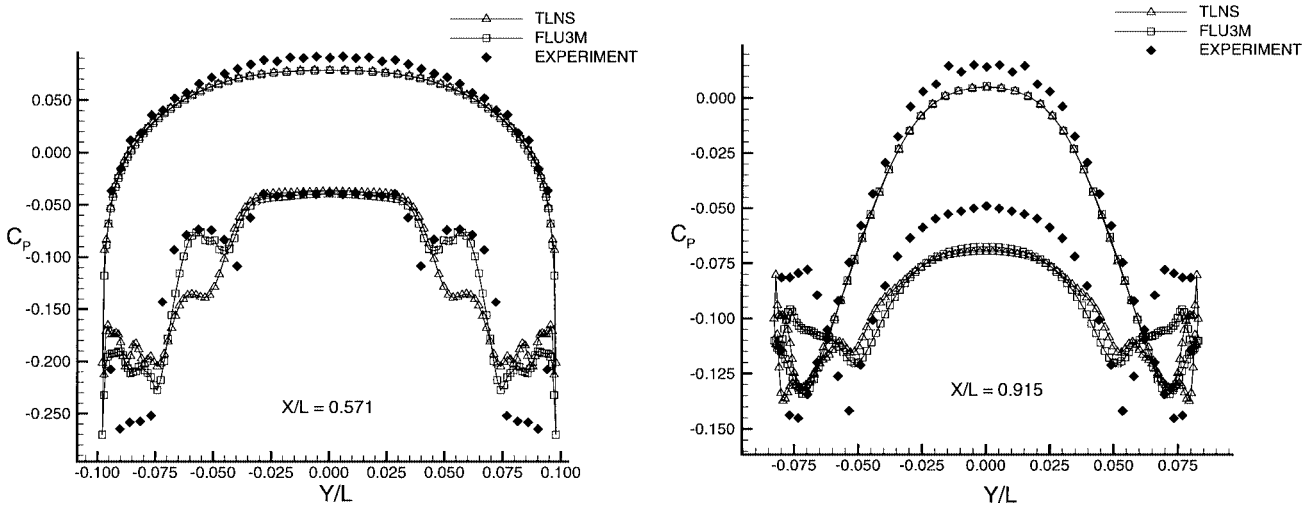

Fig. 19 Pressure coefficient distribution on the surface: $M = 2.0$, $\alpha = 10.0$ deg, and $Re_L = 3.0E6$.

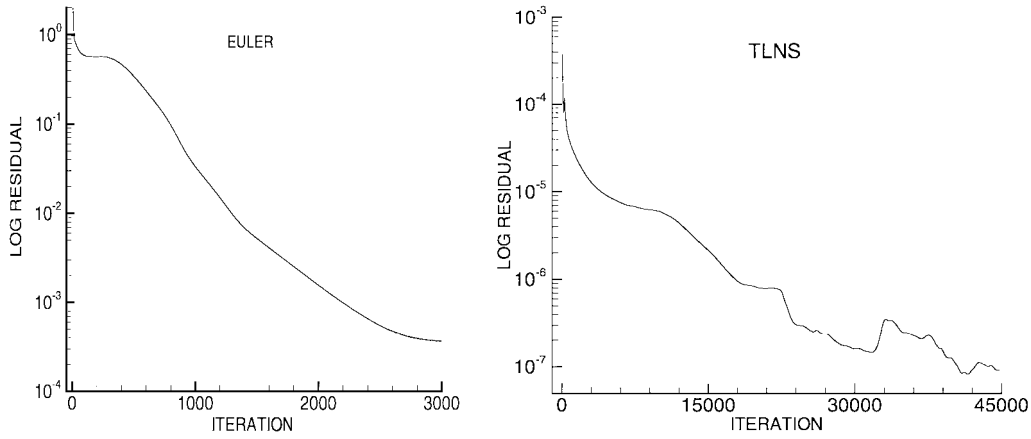

Fig. 20 Convergence history for the solution of unconventional missile geometry.

turbulence model employed. Present calculations are performed by using the original Baldwin–Lomax turbulence model without any modifications. However, to account for the complex vortical structures found in this highly separated flow region, the Baldwin–Lomax turbulence model must be modified. As stated in Ref. 5, with these modifications made to the Baldwin–Lomax turbulence model, it was possible to predict accurately the high incidence flow.

Typical convergence histories for USER3D and TLNS solvers are given in Figs. 20a and 20b. For unconventional missile geometry, the USER3D solutions were obtained with approximately 3000 time iterations for a reduction of about 3.5 orders of magnitude in the total average residuals. Typical runtimes are about 17 h of CPU time on a Hewlett–Packard 730 workstation, 8.5 h on a Hewlett–Packard-C110 workstation, or 4 h on a single-processor Silicon Graphics, Inc., ORIGIN2000 parallel machine. However, the TLNS solution for the same geometry takes about 250 h on the single processor of the ORIGIN2000 parallel machine at the end of 45,000 time steps with different Courant–Friedrichs–Lewy (CFL) numbers (20,000 iterations with CFL = 0.1, next 10,000 iterations with CFL = 0.5, and then 15,000 iterations with CFL = 1.0) to achieve 3.6 orders of magnitude of reduction in the total average residual.

Conclusions

The main emphasis has been on the TLNS computational results for the conventional and unconventional missile geometries for which Euler results have already been presented.[2] The TLNS results are compared with previous Euler and Navier–Stokes solutions from ONERA, as well as their experimental results.

The aerodynamic force and moment coefficients for the conventional and the unconventional missile geometries calculated with the present Euler and TLNS codes are found to agree well with the calculations of ONERA's Navier–Stokes solver as well as with their experimental data. The detailed flowfield predictions of the present TLNS solver showed slight discrepancies with the experimental data. Several interesting features of this vortical flow are evidenced, such as the existence of two corotating vortices: the inner and the outer vortices, the domination of the sharp edge vortex (outer vortex), and their coalescing into a single vortex. These discrepancies are mainly due to the Baldwin–Lomax turbulence model used without appropriate modifications to account for the complex vortical structure in the highly separated flow region.[5] Comparison of these vortical flow structures with the available experimental results of ONERA reveals good agreement. Although thin-layer assumptions are used throughout these calculations, the physics of the vortical flowfield are surprisingly well predicted. Comparison of the computed surface skin friction lines with those of oil flow visualization provides good insight into the explanation of the separation and reattachment lines on the leeward surface. On the other hand, the predictions of Euler computations for the overall coefficients are also in good agreement with the TLNS solutions. Therefore, when the overall coefficients are the main concern, it is sufficient to solve the Euler equations. However, when details of the flowfield are required, one must solve the full or the thin-layer Navier–Stokes equations.

Acknowledgment

This work was supported by the AGARD Fluid Dynamics Panel (under Contract 656-T106). This support is gratefully acknowledged.

References

[1]Oktay, E., "USER3D, 3 Dimensional Unstructured Euler Solver," ROKETSAN Missile Industries, Inc., SA-RS-RP-R 009/442, Ankara, Turkey, May 1994.

[2]Oktay, E., Alemdaroğlu, N., Tarhan, E., Champigny, P., and d'Espiney, P., "Unstructured 3D-Euler Computations for Missile at Supersonic Speeds and High Angles of Attack," AIAA Paper 98-0392, Jan. 1998.

[3]Schiff, L. B., and Steger, J. L., "Numerical Simulation of Steady Supersonic Viscous Flows," *AIAA Journal*, Vol. 18, No. 12, 1980, pp. 1421–1430.

[4]Degani, D., and Schiff, L. B., "Numerical Simulation of Steady Supersonic Flows Around Pointed Bodies Having Crossflow Separation," *Journal of Computational Physics*, Vol. 66, No. 1, 1986, pp. 173–196.

[5]Schiff, L. B., Degani, D., and Cummings, R. M., "Computation of Three-Dimensional Turbulent Vortical Flows on Bodies at High Incidence," *Journal of Aircraft*, Vol. 28, No. 11, 1991, pp. 689–699.

[6]Degani, D., Schiff, L. B., and Levy, Y., "Physical Considerations Governing Computation of Turbulent Flows over Bodies at Large Incidence," AIAA Paper 90-0096, 1990.

[7]d'Espiney, P., "Comparaison de Differentes Methodes de Calcul Appliquees a un Fuselage de Section Lenticulaire," CP-493, AGARD, 1990, pp. 17.1–17.15.

[8]Borrel, M., d'Espiney, P., and Jouet, C., "Three Dimensional Thin Layer and Space Marching Navier–Stokes Computations Using an Implicit MUSCL Approach: Comparison with Experiments and Euler Computations," ONERA, TP-1991-131, Chatillon CEDEX, France, 1991.

[9]Jouet C., and d'Espiney, P., "3D Laminar and 2D Turbulent Computations with the Navier–Stokes Solver FLU3M," ONERA, TP-1993-105, Chatillon CEDEX, France, 1993.

[10]Champigny, P., "Test Data on a Non-Circular Body for Subsonic, Transonic and Supersonic Mach Numbers," *A Selection of Experimental Test Cases for the Validation of CFD Codes*, Advisory Rept. 303, AGARD, Vol. 2, Aug. 1994, pp. C6.1–C6.11.

[11]Roe, P. L., "Characteristic-Based Schemes for the Euler Equations," *Annual Review of Fluid Mechanics*, Vol. 18, 1986, pp. 337–365.

[12]Jameson, A., and Baker, T. J., "Solution of the Euler Equations by Finite Volume Methods Using Runge–Kutta Time Stepping Schemes," AIAA Paper 81-1259, June 1981.

[13]Beam, R., and Warming, R. F., "An Implicit Finite Difference for Hyperbolic System in Conservation-Law Form," *Journal of Computational Physics*, Vol. 22, Sept. 1976, pp. 87–110.

[14]Pulliam, T. H., and Chaussee, D. S., "A Diagonal Form of an Implicit Approximate-Factorization Algorithm," *Journal of Computational Physics*, Vol. 39, No. 2, 1981, pp. 347–363.

[15]Kaynak, Ü., and Flores, J., "Advances in the Computation of Transonic Separated Flows over Finite Wings," AIAA Paper 87-1195, June 1987.

R. M. Cummings
Associate Editor